metals

MDPI

Article

Adjustable Elasticity of Anatomically Shaped Lattice Bone Scaffold Built by Electron Beam Melting Ti6Al4V Powder

Jelena R. Stojković [1], Miloš Stojković [1], Rajko Turudija [1], Jovan Aranđelović [1] and Dragan Marinkovic [1,2,*]

[1] Faculty of Mechanical Engineering, University of Niš, Aleksandra Medvedeva 14, 18000 Niš, Serbia; jelena.stojkovic@masfak.ni.ac.rs (J.R.S.); milos.stojkovic@masfak.ni.ac.rs (M.S.); rajko.turudija@masfak.ni.ac.rs (R.T.); jovan.arandjelovic@masfak.ni.ac.rs (J.A.)
[2] Department of Structural Analysis, Technical University of Berlin, 10623 Berlin, Germany
* Correspondence: dragan.marinkovic@tu-berlin.de

Abstract: This study investigates the elasticity of specific lattice structures made from titanium alloy (Ti6Al4V), namely, anatomically shaped lattice scaffolds (ASLS) aimed for reinforcement of the bone tissue graft that substitute a missing piece of the previously injured bone during its recovery. ASLSs that were used for testing were fabricated using the Electron Beam Melting (EBM) method. The mechanical properties of the ASLS were examined through uniaxial compression tests. Compression testing revealed the complex non-linear behavior of the scaffold structure's elasticity, with distinct compression stages and deformation dependencies. The ASLS structures exhibited quasi-elastic deformation followed by the rupture of individual struts. Results demonstrate that the ASLSs can be stiffened by applying appropriate compression load and accordingly achieve the target elasticity of the structure for the specific load range. The modulus of elasticity was determined for different compression stages of ASLS, allowing interpolation of the functional relation between the modulus of elasticity and compressive force that is used for stiffening the ASLS. This study enhances the understanding of the mechanical behavior of the specific lattice structures made of Ti6Al4V and provides insights for the development of mechanically optimized anatomically shaped lattice scaffolds.

Keywords: titanium alloy; lattice structure; EBM; bone tissue scaffold; compression

check for updates

Citation: Stojković, J.R.; Stojković, M.; Turudija, R.; Aranđelović, J.; Marinkovic, D. Adjustable Elasticity of Anatomically Shaped Lattice Bone Scaffold Built by Electron Beam Melting Ti6Al4V Powder. *Metals* **2023**, *13*, 1522. https://doi.org/10.3390/met13091522

Academic Editors: Abdollah Saboori and Pavel Krakhmalev

Received: 28 June 2023
Revised: 25 August 2023
Accepted: 26 August 2023
Published: 27 August 2023

Copyright: © 2023 by the authors. Licensee MDPI, Basel, Switzerland. This article is an open access article distributed under the terms and conditions of the Creative Commons Attribution (CC BY) license (https://creativecommons.org/licenses/by/4.0/).

1. Introduction

Titanium and its alloys are highly utilized in the production of medical implants, scaffolds, and other medical devices due to their exceptional mechanical properties, biocompatibility, and resistance to corrosion [1–3]. Tissue engineering, a promising field, involves the application of biomaterials to regenerate damaged tissues and organs. In this context, scaffolds play a crucial role by providing structural support for tissue growth and offering mechanical assistance during the regeneration process.

The introduction of additive manufacturing (AM) has revolutionized the manufacturing process of implants and scaffolds, enabling the production of intricate geometries and customized components [4]. Various AM technologies, including Electron Beam Melting (EBM), Direct Metal Laser Sintering (DMLS), and Selective Laser Melting (SLM), have been employed to fabricate titanium implants and scaffolds with tailored mechanical properties [1,5–12].

However, the mechanical properties and functionality of tissue engineering scaffolds are significantly influenced by their design. Researchers have extensively investigated the impact of different scaffold designs, such as open and closed cell structures, on the mechanical properties of titanium alloy scaffolds used in tissue engineering [13–17]. These studies explore how the scaffold's geometry and porosity can affect mechanical properties, such as compressive strength and elastic modulus. Additionally, apart from the pore

structure, the porosity and mechanical properties of tissue engineering scaffolds can be influenced by various factors, such as material composition, surface modifications, and manufacturing process. The choice of manufacturing method, in particular, can have a substantial impact on the resulting scaffold properties [11,12,18]. Adjusting the processing parameters of the manufacturing method, such as laser power and scanning speed, enables control over scaffold porosity. Similarly, the mechanical properties of the scaffold can be tailored by adjusting design parameters, such as strut thickness and pore size.

For example, two review papers Distefano et al. [19] and Raheem et al. [20] highlight the ongoing efforts to optimize the mechanical and morphological properties of titanium scaffolds for bone replacements. By addressing challenges related to pore size, surface roughness, and elastic modulus, as well as leveraging additive manufacturing and biomimetic principles, researchers are advancing the development of more effective and biocompatible implants for enhanced osteointegration. Distefano et al. [19] focused on Ti6Al4V porous scaffolds, aiming to provide a comprehensive summary of the mechanical and morphological requirements for successful osteointegration. The study highlighted the influence of pore size, surface roughness, and elastic modulus on the performance of bone scaffolds. Porosity and pore size were identified as major challenges, with a wide range of optimal pore sizes reported in the literature, varying from 100 to 1000 µm. These discrepancies underscore the complexity of achieving the ideal scaffold architecture for biomedical applications. Furthermore, the review emphasized the importance of reducing the implant stiffness to mimic the mechanical properties of human bone. Lowering the elastic modulus of the implant has been shown to improve stress stimulation and reduce stress shielding, a phenomenon that arises when implants characterized by a high elastic modulus and tensile strength result in an uneven distribution of bodyweight, potentially leading to long-term bone loss or osteopenia. In the second review paper, Raheem et al. [20] delved into the utilization of additive manufacturing and biomimetic principles in the fabrication of ceramic, polymer, and metal implants. It highlighted the ability of additive manufacturing techniques to create implants with exceptional resemblance to natural tissue. However, similar challenges were identified by Distefano et al. [19], as higher elastic modulus of these implants leads to stress shielding and potential complications in the long term. To address this issue, researchers have shifted their focus towards functionally graded materials (FGM), which allow for varying lattice arrangements and adaptive porosity. This approach has the potential to mimic the complex architecture of natural bone more closely, according to the authors. Additionally, Raheem et al. [20] depict that various conventional manufacturing techniques fall short in replicating the physical and mechanical properties of natural human bone, thus, additive manufacturing of hard metals has emerged as a superior method in the field of biomimetics.

Several studies have explored the utilization of Selective Laser Melting (SLM) technology for the fabrication of porous scaffolds made from Ti6Al4V material, with the aim of achieving optimal mechanical properties and functionality [16,21–23]. Mondal et al. [21] focused on the fabrication of four different porous scaffolds—diamond, grid, cross, and vinties—while maintaining a theoretical porosity of 65%. The mechanical performance of each scaffold was evaluated through compression tests. The elastic modulus of the fabricated samples closely matched that of human bone. Additionally, the compressive strength of the scaffolds exceeded that of human bone, which, according to authors, indicated a potential reduction in the stress-shielding effect and improved implant longevity. The diamond, cross, grid, and vinties scaffolds exhibited elastic moduli of 10.08, 11.15, 10.33, and 11.76 GPa, respectively, and the corresponding compressive strengths were observed as 79.685, 78.735, 75.1, and 79.328 MPa, respectively. Hudak et al. [16] conducted a comprehensive examination of the mechanical properties of six series of samples differing from each other in terms of pore size (ranging from 200 to 600 µm) and porous structure topology (cubic or trabecular). Static compressive tests were employed as the evaluation method. It was found that the samples with a trabecular structure and a pore size of 600 µm achieved the highest porosity and lowest weight. However, samples with a pore

size of 200 µm and a cubic structure exhibited the best mechanical properties. Trabecular structures with larger pores were identified as the most suitable for producing biomaterials with mechanical properties comparable to human bone. Loginov et al. [22] conducted a study to investigate the ductility and fracture behavior of additively manufactured Ti6Al4V samples with a lattice structure based on modified diamond-shaped (tetrahedral) basic cell elements specifically designed for osteosynthesis purposes. The focus of the research was to analyze samples with varying porosities of 50%, 60%, 70%, and 80%. The study revealed that the compressive strength of the samples decreased as the porosity increased, which is also the case with papers [16,21]. Additionally, Loginov et al. [22] examined the compressive offset stress (σ0.2), which represents the compressive stress at a plastic compressive strain of 0.2%. The study found that the compressive offset stress decreased approximately 12 times across the porosity range of 50% to 80%, ranging from 138 to 11 MPa. Similarly, in the study conducted by Dhiman et al. [23], where Ti6Al4V cubic Porous Lattice Structure (PLS) scaffolds were analyzed using finite element (FE) analysis and fabricated through the selective laser melting (SLM) technique, the PLS scaffolds with the smallest pore size (of 600 µm) and an overall relative density (RD) of 57% exhibited the highest ultimate compressive strength, reaching 119 MPa. However, it is noteworthy that the study also identified a particular issue related to the fabrication process. The failure of the scaffold structure was observed to initiate from micro-porosities formed during the fabrication process. These micro-porosities were attributed to improper melting along a plane inclined at a 45-degree angle. This was also reported in numerous other studies, not only dealing with SLM but also with EBM technology, by Zhang et al. [24] and Del Guercio et al. [25]. This observation highlights the importance of precise control and optimization of the fabrication parameters to minimize structural defects and enhance the overall quality of the scaffolds. Bari et al. [17] investigated the suitability of four lattice topologies as implants for segmental bone defect replacements. The study focused on designing and manufacturing lattice structures using direct melt laser sintering (DMLS). The four lattice topologies explored were BCC (Body-centered cubic), FCC (Face-centered cubic), AUX (Auxetic negative Poisson ratio), and ORG (Organic cancellous bone). The results revealed that the ORG, FCC, and BCC lattice structures exhibited the highest strength values, ranging from 25 to 30 MPa before failure. However, the strengths inside the linear deformation of these structures varied from 4 to 17 MPa. The Young's modulus was determined to be 1.4784 GPa for BCC, 2.5881 GPa for FCC, 1.9708 GPa for AUX, and 3.0405 GPa for ORG scaffolds. Kotzem et al. [26] conducted a study focusing on the manufacturing of Ti6Al4V lattice structures using Electron Beam Melting (EBM) technology. The research aimed to investigate the influence of microstructural features on the mechanical behavior of these lattice structures. Two different lattice types were selected based on their deformation behavior: body-centered cubic-like (BCC) and face-centered cubic-like (F2CCZ) structures. The results revealed distinct mechanical characteristics between the BCC and F2CCZ lattice structures. The BCC lattice exhibited a more ductile material behavior, characterized by higher fracture strain and higher load-bearing capacity, with the ability to sustain approximately 93% of the initial peak stress after initial failure. On the other hand, the F2CCZ lattice structures demonstrated higher fatigue strength during cyclic testing. However, it is important to note that the as-built surface roughness of the lattice structures played a significant role in their performance during the cycle testing. The rough surface contributed to early failure, as multiple crack initiation sites were observed on the specimen surfaces. The study conducted by Parthasarathy et al. [27] investigates the microstructural analysis and mechanical characterization of porous Ti6Al4V structures fabricated using the electron beam melting (EBM) process. Utilizing this technique, parts with porosities ranging from 49.75% to 70.32% were successfully manufactured. The resulting structures exhibited pore sizes ranging from 765 to 1960 µm and strut sizes of 466 to 941 µm. By comparing two samples with similar porosity levels of 49.75% and 50.75% but varying strut thicknesses, it was observed that compressive stiffness and strength decreased significantly. The stiffness had an 80.5% reduction, while the strength decreased to 93.54%. This indicates that the strength

of the lattice structure was influenced not only by the overall porosity values but also by the geometric dimensions of the solid struts. According to the authors, this study showed EBM to be a promising process for the fabrication of patient-specific custom implants with predictable mechanical properties, which is in line with what Zumofen et al. [28] concluded in their study. De Pasquale et al. [29] conducted an evaluation of lattice failure under compressive loads, considering the process typology, material properties, and dimensional parameters of cubic unit cells produced via SLM and EBM machines within a cubic volume. This study identified three modes of lattice collapse during compression testing: The first mode, observed in both SLM and EBM samples, is characterized by buckling at the intersection of struts, where the applied load leads to instability in vertical struts at the intersection point. The second mode, observed exclusively in EBM samples, involves brittle fractures of horizontal struts caused by shear forces. The third mode combines the previous two modes, seen only in EBM samples. Sepe et al. investigated the effects of dimensions, building position, and orientation on the mechanical properties of EBM octet cell lattice scaffolds within a standard cylindrical specimen. The study included three different strut diameters (1, 1.5, 2 mm) and orientations (0°, 45°, 90°), as well as the position on the build plate. In contrast to the previous study by De Pasquale et al. and most papers on this topic, Sepe et al. [30] conducted a tensile test. The specimens printed at a 45° orientation exhibited superior mechanical behavior. Additionally, an increase in mechanical strength was observed with larger strut diameters. Notably, samples printed at the center of the build plate demonstrated greater stiffness compared to those printed in the corners. Similarly, Suard et al. [31] explored the effects of build angles (0°, 45°, 90°) on single struts (1 mm diameter, 15 mm length) of lattice scaffolds produced using an EBM machine. This study involved uniaxial compression tests, which were then compared to Finite Element Analysis (FEA) results. Discrepancies between the results were attributed to differences between the dimensions of the struts in the CAD model and the printed struts. The study suggests a solution to this issue by employing an equivalent strut diameter. Cansizoglu et al. [32] conducted compression and bending tests on hexagonal cell lattice scaffolds produced using EBM. The study revealed that, across all unit cell sizes, specimens loaded in parallel exhibited greater stiffness and strength, and required less work to fail compared to specimens loaded perpendicularly. This aligns with findings from previous studies, which indicated that mechanical performance decreases with an increase in cell size. A 3-point bending test demonstrated that reducing the unit cell size resulted in an increase in the flexural modulus value. Del Guercio et al. [33] investigated the impact of three different lattice scaffold cell geometries and various dimensions (unit cells: 4, 7, 10 mm) on the mechanical properties of EBM-printed lattice scaffolds. The study utilized three standard Materialize Magics database cell structures: Dode Thin, G-Structure 3, and Rombi Dodecahedron. Similar to previous research, this study found that larger cell sizes led to decreased mechanical performance. Compression tests also revealed that the Dode Thin cell structure exhibited the poorest mechanical properties, followed by the Rombi Dodecahedron structure, while the G-Structure 3 demonstrated the best mechanical performance. Additionally, the study highlighted that unit cell size has a more significant influence on mechanical properties than unit cell type. Ataee et al. [34] evaluated the mechanical behavior of gyroid cell EBM lattice scaffolds with three different unit sizes (2, 2.5, and 3 mm). Through mechanical compression testing, the study determined that the elastic modulus of these gyroid scaffolds ranged from 637 to 1084 MPa, while the yield strength ranged from 13.1 to 15.0 MPa, similar to trabecular bone properties. Numerous studies have indicated a disparity between nominal CAD dimensions and actual measured dimensions of printed lattice scaffolds, which, combined with surface roughness, affects mechanical performance [29–31]. Galati et al. [35] explored the effects of post-treatment on the mechanical properties of titanium dodecahedral cell lattice scaffolds produced via EBM within a cylindrical volume. Three different cell sizes were subjected to uniaxial compression testing, confirming that increased cell size led to reduced compressive strength. The application of heat treatment had an insignificant impact on Young's modulus but caused a

slight reduction in ultimate compression strength and a smoother stress-strain curve with fewer drops. Moreover, heat-treated samples exhibited ductile behavior, unlike the brittle behavior of untreated samples. This research also revealed that the maximum stress before steep drop (scaffold failure) had a higher value for heat-treated samples.

In addition to conventional open-cell and closed-cell scaffold designs, there also exist various scaffold designs that do not fall into these categories [13]. These unique designs often have distinct pore structures and geometries that can significantly impact their mechanical properties and functionality. It would be valuable to investigate the mechanical behavior of these unique scaffold designs under compression and elastic modulus tests, as well as how their mechanical properties are influenced by different additive manufacturing techniques used to produce them.

When discussing anatomically shaped lattice scaffolds (ASLS) [36–38], it is important to understand that the ASLS structure should achieve three fundamental functions:

1. Reinforcing the liquid material of the bone graft, which, similar to its own provisional bone tissue, should transform during the recovery process into mature and healthy bone tissue and connect with the surrounding bone.
2. Forming the volume of the bone graft into the desired anatomical shape of the future bone tissue, corresponding to the anatomy of the missing bone part.
3. Enabling the targeted elastic deformation of the volume of the bone graft is crucial for the design of an ASLS. In fact, the elasticity of the ASLS needs to adapt to the loading that the patient's bone will undergo during recovery. The appropriate elastic deformation, or strain, of the ASLS and the bone graft within is of utmost importance for accelerating the process of ossification (bone formation) or transformation of provisional bone tissue into mature bone tissue. Therefore, one of the goals of designing the ASLS is to ensure the desired strain, i.e., the targeted elastic deformation of the ASLS for the most common loading scenario during recovery, through suitable design and construction.

In this context, it is crucial to investigate the elasticity of lattice structures made from titanium alloys, specifically Ti6Al4V, which are commonly employed in scaffolds for bone replacements due to their biocompatibility. The focus of the study was to explore the mechanical properties of an ASLS fabricated using the EBM process. Compression testing was conducted on the EBM-fabricated ASLS scaffolds intended for the restoration of a missing part of the rabbit tibia. The evaluation specifically considered uniaxial compression, a typical loading scenario in tibial bone replacements. The utilization of optimal manufacturing techniques, such as EBM, played a crucial role in this investigation.

2. Materials and Methods

A scaffold model was designed in the CATIA computer-aided design (CAD) software. The model is based on a CT scan of a rabbit. A portion of the tibia bone is cut out, and inside this volume, the scaffold is designed using reverse engineering (RE) methods. The outer struts have a diameter of 0.4 mm, while the inner struts have a diameter of 0.32 mm as the primary load transfer goes through the cortical bone.

Ti6Al4V ASLS were produced using EBM (Arcam A1, Mölnlycke, Sweden). EBM is an AM process that utilizes a high-energy electron beam to melt metal powder layer by layer. The process takes place within a vacuum environment, which preserves the material's chemical composition and is particularly suitable for reactive materials, such as titanium alloys. The electron beam's substantial power ensures uniform temperature distribution, enabling full melting of the metal powder and resulting in high-strength properties of the material.

The Arcam A1 is an EBM machine that employs gas-atomized powder with particle sizes ranging from 45 to 100 microns, ensuring safe powder handling during the printing process. The key process parameters utilized on the Arcam A1 machine are presented in Table 1.

Table 1. Parameters used in EBM process on the Arcam A1.

Parameters	ARCAM A1 (EBM)
Energy source	50–3000 W (electron beam)
Min. Beam size	200 µm
Environment	Vacuum
Layer thickness	70 µm
Print speed	4 mm/h
Scan speed	1500 mm/s

The EBM process works in a vacuum environment and at high temperatures, which ensures small thermal shrinkages and a high degree of consistency of the non-melted powder. The preheating step that precedes the process achieves a temperature of approximately 650–700 °C for Ti6Al4V in the work chamber. The elevated build temperature employed in the manufacturing process results in stress-relieved Ti6Al4V parts with the desired a/ß-microstructure, eliminating the need for additional heat treatment or support structures. This enables the seamless production of micro-architectured materials. Post-processing was minimal, limited to the removal and recycling of excess powder using the Powder Recovery System. Remarkably, these parts were built entirely without the utilization of support structures.

The titanium Ti6Al4V powders (Arcam AB, Mölnlycke, Sweden) utilized in the process were provided by the machine manufacturers, and their chemical composition and mechanical properties are detailed in Tables 2 and 3.

Table 2. Chemical composition of Ti6Al4V powder used in the EBM process.

Technologies	Aluminium (Al)	Vanadium (V)	Iron (Fe)	Oxygen (O)	Nitrogen (N)	Carbon (C)	Hydrogen (H)	Titanium (Ti)
EBM Arcam A1 Ti-6Al-4V	5.5–6.5%	3.5–4.5%	<0.30%	<0.20%	<0.05%	<0.08%	<0.015%	Balance

Table 3. Mechanical properties of Arcam Titanium Ti6Al4V powder used in the EBM process.

Mechanical Properties	Arcam Titanium Ti6Al4V (Grade 5) Powder
Ultimate Tensile Strength,	951 MPa
Yield Strength, $Rp_{0.2}$	1020 MPa
Fatigue Strength @ 600 MPa	>10,000,000 cycles
Elongation at Break	14%
Modulus of Elasticity	120 GPa
Rockwell Hardness	33 HRC

High temperatures eliminated the need for additional heat treatment while simultaneously causing the Ti parts to "snap off" the build plate (due to the difference in thermal coefficient), rendering the use of sawing or EDM unnecessary for the removal of EBM-manufactured parts. The scaffolds made with EBM technology are shown in Figure 1.

A specialized custom-made tool with a seating mechanism has been developed to minimize any initial displacement during the compression test. This tool is designed to provide stability and ensure accurate testing conditions from the start. The illustration of this custom-made tool is shown in Figure 2.



Figure 1. Anatomically shaped lattice Ti6Al4V scaffold specifically designed to address large trauma in the proximal diaphysis of a rabbit's tibia fabricated by EBM.

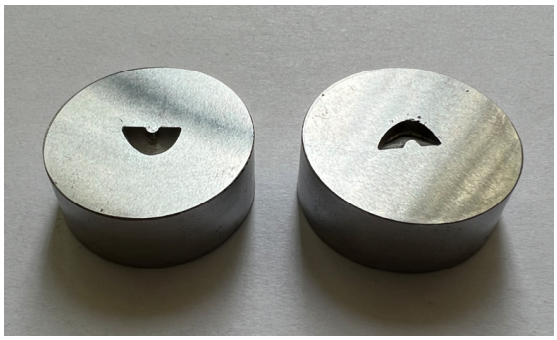


Figure 2. Custom-made tool for scaffold compression testing.

The Shimadzu Table-top AGS-X 10kN universal testing machine (Shimadzu, Kyoto, Japan) was used for conducting compressive testing. This machine consists of essential components, such as a rigid frame, a movable crosshead, test fixtures (jaws) for specimen gripping, force sensors, and a control unit. Figure 3a provides an illustration of the universal testing machine, while Figure 3b displays examples of the tested specimens.



(**a**) (**b**)

Figure 3. Experimental setup: (**a**) Shimadzu Table-top AGS-X 10kN universal testing machine and (**b**) some of the specimens to be tested.

Detailed specifications for the Shimadzu Table-top AGS-X 10kN universal testing machine can be found in Table 4.

Table 4. Shimadzu Table-top AGS-X 10kN Universal Testing Machine Characteristics.

Brand	**Shimadzu**
Model	Table-top AGS-X 10 kN
Weight	85 kg
Power	1.2 kW
Max load/capacity	10 kN
Dimensions	W 653 mm × D 520 mm × H 1603 mm
Crosshead speed range	0.001 to 1000 mm/min
Crosshead speed accuracy	0.1%
Crosshead–table distance (tensile stroke)	1200 mm (760 mm, MWG)
Data capture rate	1000 Hz max

For this study, quasi-static uniaxial compression tests were carried out on ASLS scaffolds produced by the EBM technology. These tests were carried out in vitro on the aforementioned Shimadzu table-top AGS-X 10kN universal testing machine (UTM).

Firstly, a single-step compression test was carried out with a compression speed of 1 mm/min. This was done to determine the zones where the behavior of the scaffold changes (the point where plastic buckling/crushing starts, plateau force, densification, and scaffold failure point [32]).

Next, the structural performance of ASLS scaffolds was evaluated through their exposure to multiple loading-unloading steps (in the text and figures below, as a synonym for the term loading-unloading step, compression-decompression, and compression-relaxation cycles were used). This approach should indicate which trends should initially be expected in the real-life application of the ASLS scaffolds (the scaffolds are cyclically loaded and unloaded while walking). To check the elastic behavior of the scaffolds, multiple load-unload steps were carried out. Two tests were carried out with a compression speed of 1 mm/min, and an additional test was carried out with a compression speed of 0.25 mm/min to check if it influenced the results. The tests show that the compression speed does not influence the results, as the results from both tests showed the same stress-strain curve. The controlled loading-unloading procedure comprised of the following steps:

- the scaffold was compressed up to a certain force, once this force was achieved it was maintained for 2 s,
- next, the scaffold was unloaded down to a force smaller than that of the previous step (not zero, to keep the scaffold in contact with the fixtures), once this force was achieved, it was maintained for 2 s.

The entire process was repeated for multiple increasing force load increments (determined based on the first single-step compression test) (Table 5). This procedure makes it possible to determine at which point plastic deformations start.

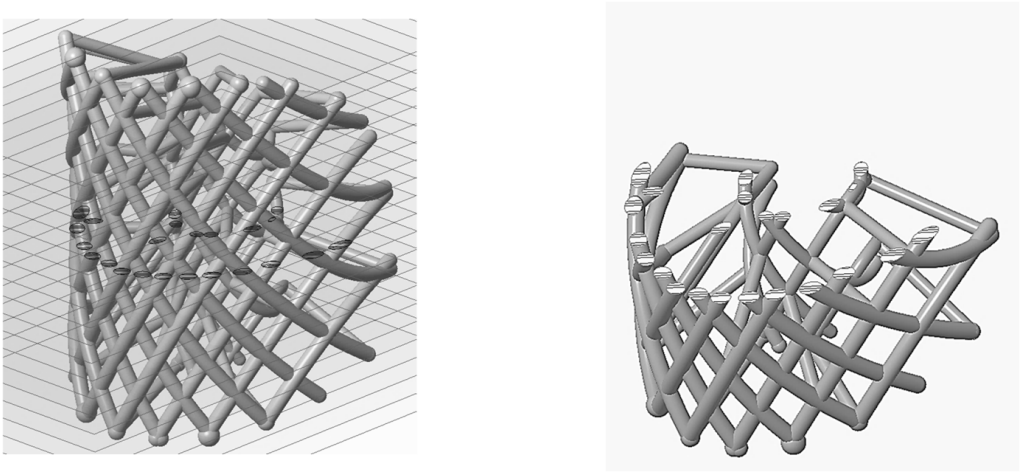
Table 5. Compression-relaxation (loading-unloading) steps.

#		**1**	**2**	**3**	**4**	**5**	**6**	**7**	**8**	**9**	**10**	**11**	**12**
	Speed (mm/min)	**F (N)**	**F (N)**	**F (N)**	**F (N)**	**F (N)**	**F (N)**	**F (N)**	**F (N)**	**F (N)**	**F (N)**	**F (N)**	**F (N)**
1	1	37 ↓[1]	5 ↑[2]	42 ↓	800 ↓	42 ↑	1300 ↓	42 ↑					
2	1	37 ↓	5 ↑	42 ↓	5 ↑	55 ↓	5 ↑	150 ↓	55 ↑	500 ↓	150 ↑	1300 ↓	5 ↑
3	0.25	37 ↓	5 ↑	42 ↓	5 ↑	55 ↓	5 ↑	150 ↓	55 ↑	500 ↓	150 ↑	1300 ↓	5 ↑

[1] The sign ↓ represents compression (loading) stroke. [2] The sign ↑ represents relaxation (unloading) stroke.

Finally, a four-cycle loading-unloading test was carried out to see if the scaffold exhibited signs of plastic hardening. The scaffold was compressed until a force of 37 N was reached, this force was maintained for 2 s and then the scaffold was unloaded down to a force of 0.1 N (still keeping the scaffold in contact with the fixtures), at which it was also maintained for 2 s.

Based on all these tests, the UTM software (1.4.0, Shimadzu Corporation, Kyoto, Japan) provided us with the force-stroke points that it recorded in 10 millisecond intervals. As the scaffold did not fall into any standard specimen category, it was not possible for the TrapeziumX UTM software to provide us with the stress-strain graph. Additionally, due to the anisotropy of the scaffold cross-section, it was difficult to determine the stress exactly. In order to get a sense of the stress, we calculated an average cross-section area based on multiple cross-sections of the CAD model of ASLS normal to the compassion axis (Figure 4). We used a set of 20 cross-sections that are offset one from another by 0.5 mm to calculate the average value of the scaffold cross-section in this direction. Therefore, we adopted this value (A_avg = 3.61 mm^2) to calculate approximate normal stress. Based on this and the starting 10 mm scaffold height (length), it was possible to create an approximation of the stress-strain graph.



(**a**) (**b**)

Figure 4. The scaffold cross-sections were obtained through the analysis of the CAD model of ASLS. (**a**) ASLS with a series of planes making a set of 20 cross-sections in the direction of compression, (**b**) a cross-section whose area (3.63949 mm^2) is almost equal to the average value (3.61 mm^2).

In addition, one should notice that the total volume of the piece of the bone that scaffold reinforces is about 220 mm^3, while the volume of the scaffold itself (all the struts) is 38 mm^3. Thus, even though for this kind of lattice structure, such ASLS, porosity is not an adequate feature as it is for porous structures (foam-like structures), for the sake of comparison, the porosity of this ASLS can be calculated as a ratio of these two volumes (38/220), thus, it is 82.7%.

3. Results

3.1. Experiment 1-Determining the Whole Range of Compression, up to 35% Deformation of Initial Length of ASLS (dx = 3.5 mm, Xo = 10 mm)

In Figure 5, two characteristic zones of scaffold compression can be observed in the F(x) diagram (force–stroke diagram). The first zone exhibits quasi-elastic deformation, while the second zone shows a series of sharp declines in force, indicating the rupturing of scaffold struts.

The focus of scaffold application lies in the first zone of compression, which can be further divided into three compression stages based on their specific F(x) dependencies (Figure 6).

Due to the specific shape of ASLS, when compression starts, the scaffold tries to fit into the seat of the mold, looking for a stable position. In this stage of compression, shown in Figure 7, the scaffold, in fact, does not bear the load yet. In this case, after 0.15 mm, a steep slope of F(x) starts indicating the appearance of the reactive force of ASLS structure due to the pressure it starts to bear.

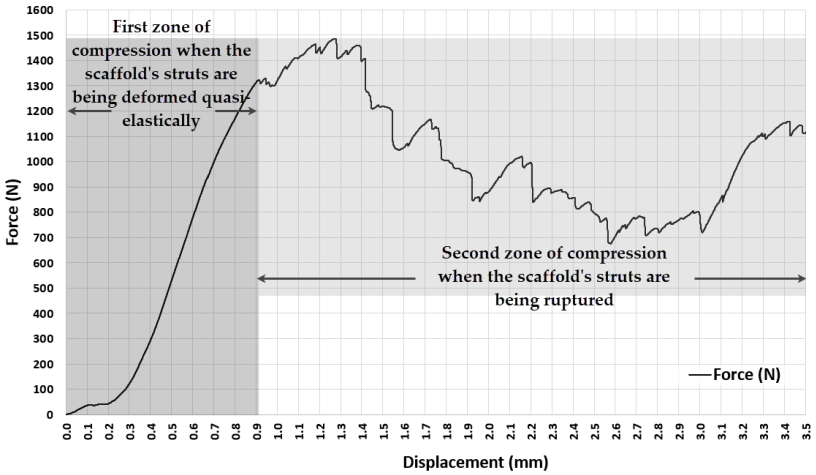


Figure 5. The whole range of compression planned by the experiment applied in one stroke.

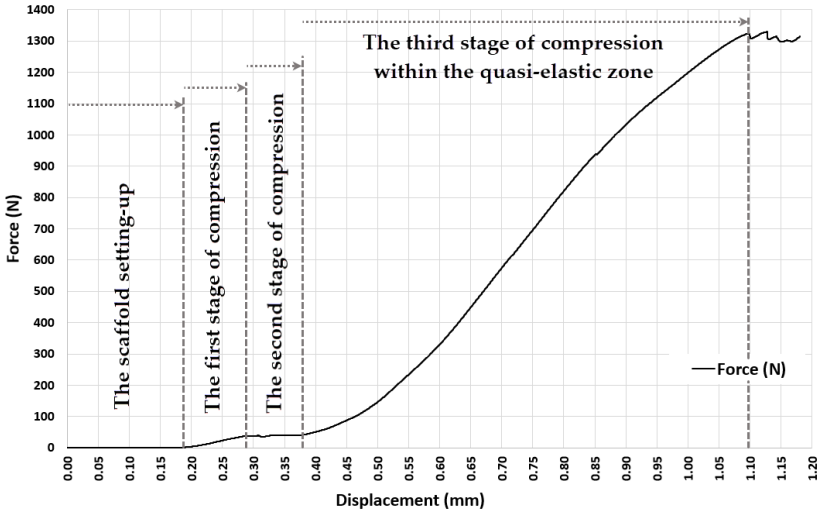


Figure 6. Three compression stages within the first zone of compression characterized by specific dF(x)/dx.

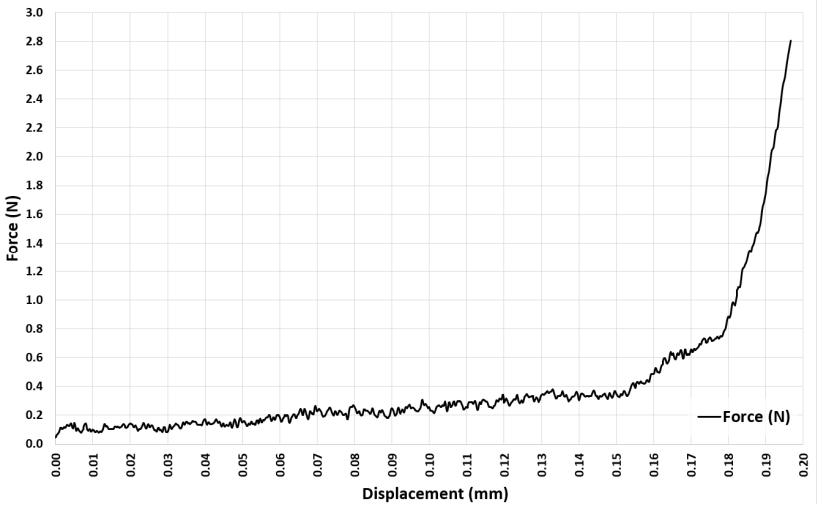


Figure 7. Fitting the scaffold into the seat of the mold.

Figure 8 shows that the first compression stage extends up to 1–1.2% of the relative deformation of the ASLS. This stage is characterized by an almost linear relationship between compression stroke and the reactive force generated by the ASLS. The second

compression stage begins after a yield point, where the reactive force of ASLS becomes almost constant despite further increases in the compression stroke. Additionally, a distinct feature of the second compression stage is a brief and slight drop in the reactive force, characterized by a sharp decline and subsequent return.

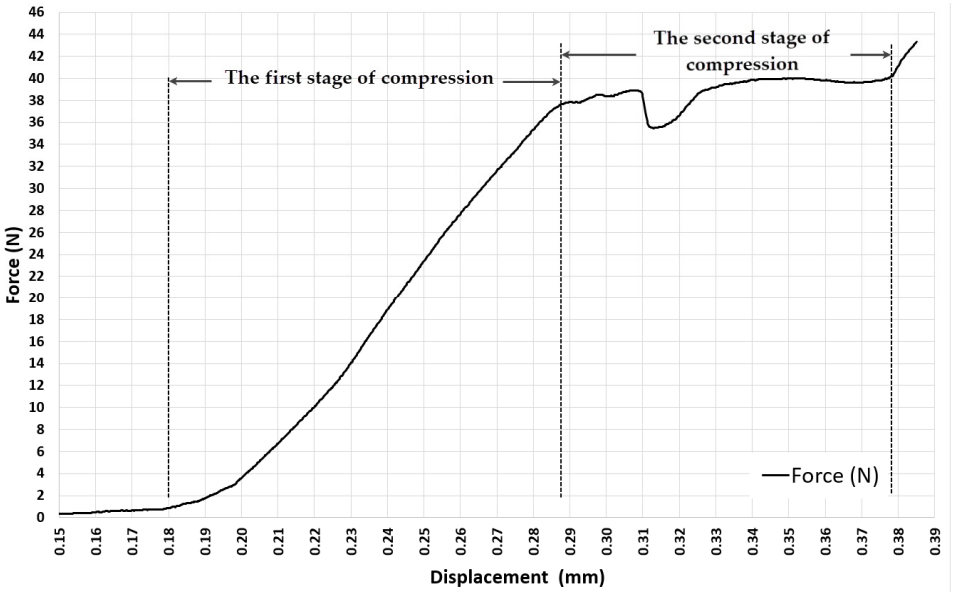


Figure 8. A closer look at the first two stages of compression, with the first stage defined between 1 and 37 N, and the second stage between 37 and 40 N.

Following the completion of the second compression stage, which represents approximately 1% of the total relative deformation of the ASLS, the third compression stage follows (as shown in Figure 9). Similar to the first stage, the third stage of compression exhibits a quasi-linear relationship between the deformation of the lattice structure and the reactive force of the ASLS. The third compression stage extends until reaching 10% of the relative deformation of the ASLS, corresponding to a range of 7.8–8% of its total deformation.

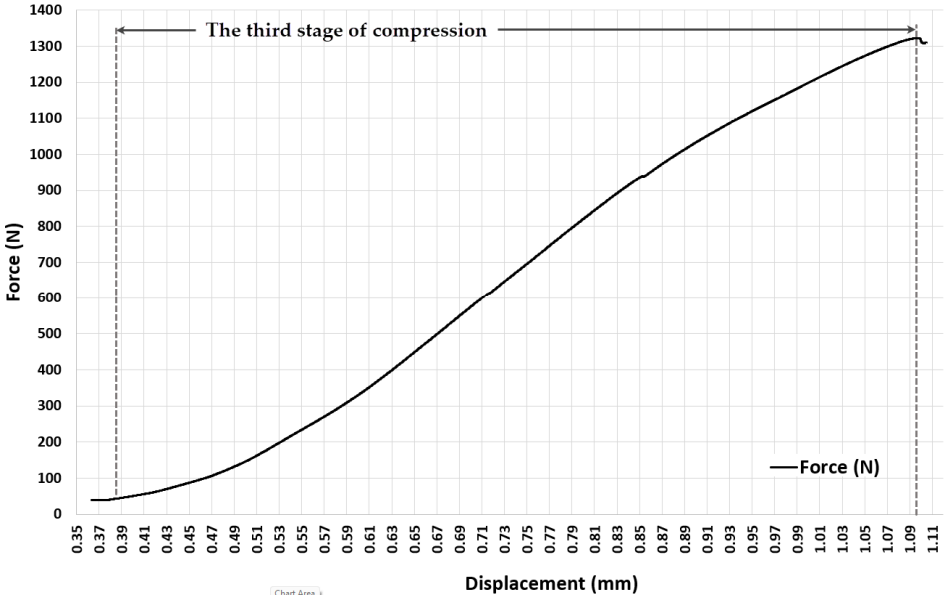


Figure 9. The third stage of compression extends from 2% to 10% of the total relative deformation of the ASLS, resulting in a reactive force range of 40 N to 1300 N.

3.2. Experiment 2–Exploring the Quasi-Elastic Properties of the ASLS for the First Compression Stage

The entire range of F(x) relation indicates the complex quasi-linearity of the scaffold structure's elasticity. However, from an application perspective, it is crucial to examine whether the ASLS structure can behave as a simple elastic structure. Therefore, we conducted several series of measurements to determine how the ASLS structure stiffness increase occurs during deformation. The tests involved relaxation (unloading) of ASLS structure after reaching the characteristic force limit of each compression (loading) phase and repeating the cycle multiple times. The compression and decompression strokes were performed at the same speed of dx/dt = 1 mm/min, i.e., 0.01667 mm/s (Figure 10).

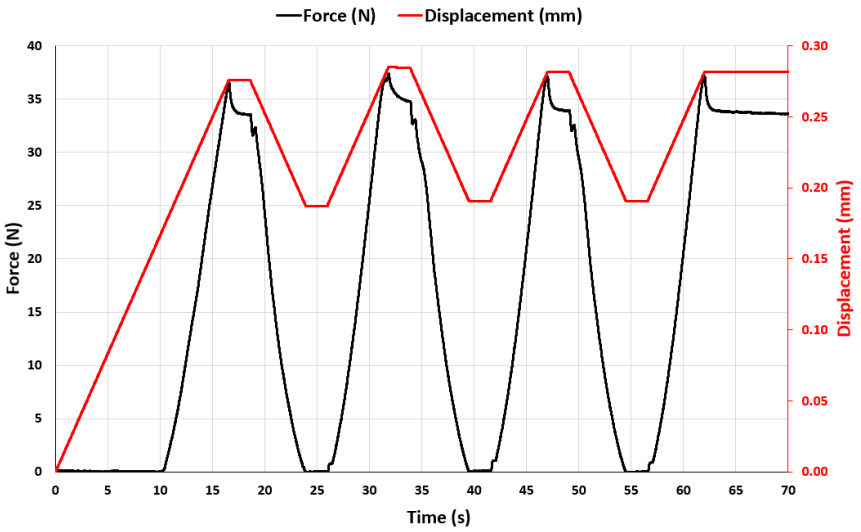


Figure 10. Compression–decompression cycles: stroke and reactive force of ASLS versus time during a series of measurements.

From Figure 11, it can be observed that after the initial compression stroke, where a compression force of 37 N (the limit of the first compression stage) is applied, the ASLS structure undergoes a deformation slightly exceeding 0.105 mm.

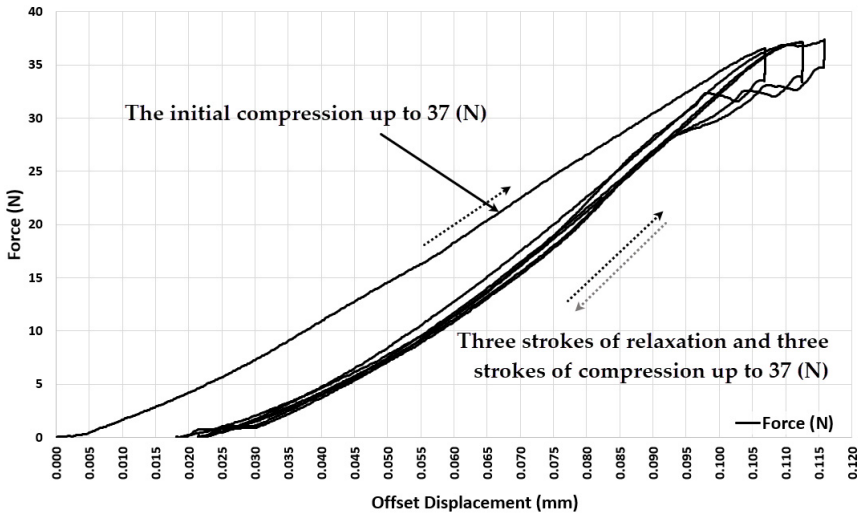


Figure 11. The diagram of compression force in function of the deformation F(x) for the first compression stroke and a series of decompression and compression strokes afterward. Arrows, which are directed upwards indicate compressive strokes, while the ones which are directed downwards, indicate relaxation strokes.

After the relaxation stroke, it becomes evident that the ASLS remains permanently deformed by approximately 0.02 mm (0.2% of the total length of ASLS). In the next three cycles of compression-decompression strokes, with compression forces up to 37 N, the ASLS demonstrates fully reversible deformation, behaving practically as an elastic structure. However, the stiffness of the ASLS is increased in comparison to the structure before and during the initial deformation.

Considering the complexity of the ASLS design, precise determination and calculation of stresses within the structure of the ASLS struts were challenging. To provide some orientation, an "orienting stress" was calculated for an imaginary structure of a single, wider strut exposed to pressure, equivalent to the sum of the cross-sections of ASLS struts made in the compression direction. The stress within the ASLS strut's structure was approximately calculated as the ratio between the measured reactive force and the average initial cross-section (made in the compression direction) of the ASLS, which is 3.61 mm^2. It is important to note that this is an approximate calculation used as an orientation value. The principal deformation of the ASLS is primarily caused by torsion in the joints of the scaffold's struts, and strut fracture results from the high shear stresses induced by this torsion. For an ASLS that rigidifies by applying the initial compression stage limit force of 37 N (without crossing the yield point), a portion of the stress-strain diagram calculated this way can be used to determine the modulus of elasticity (Figure 12). The calculated value of the modulus of elasticity for a series of ASLSs ranges from 1450 to 1850 N/mm^2.

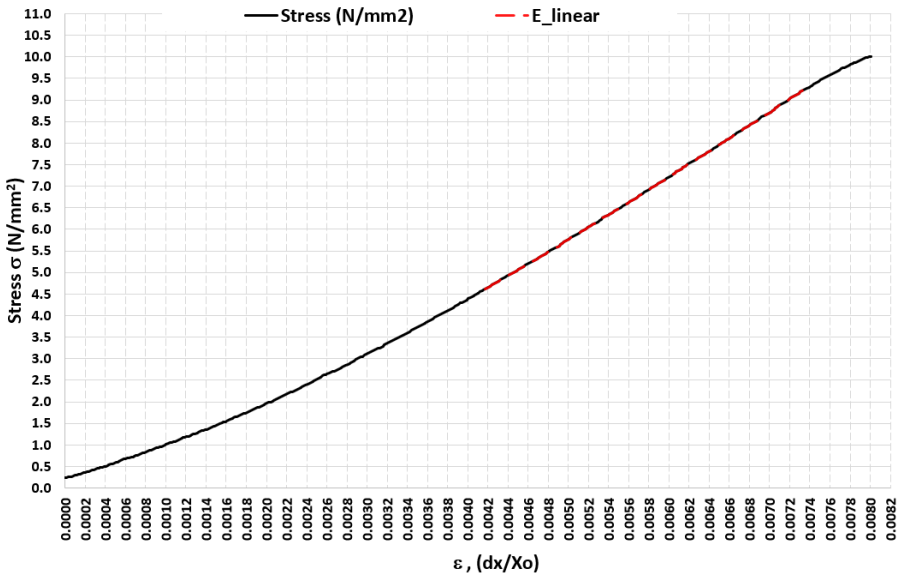


Figure 12. The diagram of the approximately calculated normal stress (σ) in function of strain (ε) for the first stage, i.e., after stiffening the ASLS. E ≈ 1479 N/mm^2, $\sigma_{_after_initial_stiffening}$ (ε) = 1479·ε.

3.3. Experiment 3-Exploring the Quasi-Elastic Properties of the ASLS throughout the Entire Range of Compression, Including the Second and Third Compression Stages

The first stage of compression is followed by the second stage, which is characterized by a significant increase in ASLS deformation compared to a small increase in the compression force. This can be described as a kind of structural yielding. However, the resulting permanent deformation of the scaffold caused by this compression stage is disproportionately low compared to the stroke that is applied. In fact, the ASLS exhibits almost fully reversible deformation once again. It is important to notice that no collapse of a strut is detected during the second stage of experiments. Additionally, the relationship between the reactive force of the ASLS on compression and its deformation during the compression stroke maintains a similar slope as observed after the initial stiffening caused by applying the force limit of the first compression stage (Figure 13).

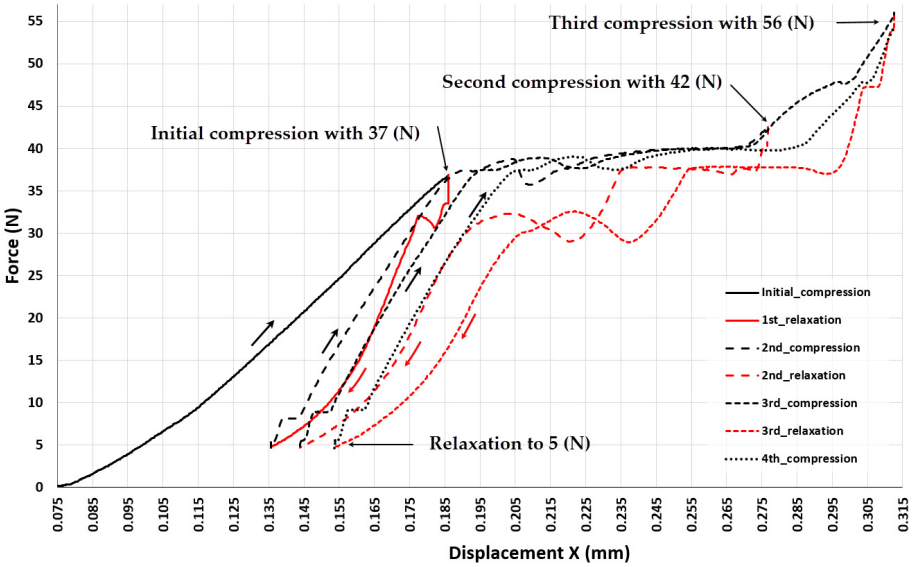


Figure 13. The diagram of the force F(x) for the case of series of compression/decompression (relaxation) strokes with corresponding small increase of the limit force. Black arrows, which are directed upwards, indicate compressive strokes, while the red ones, which are directed downwards, indicate relaxation strokes.

Figure 13 displays two interesting features of the ASLS. Firstly, each increase in compression force leads to a further increase in permanent deformation of the ASLS. However, it appears that each subsequent permanent deformation gained after relaxation does not fully account for the deformation produced by the compressive forces of the second stage of compression. This suggests a situation where the ASLS structure experiences a kind of "elastic creeping" during the second compression stage. Secondly, the slope of F(x) during the compression strokes up to the first stage limit force (37 N) remains almost the same after each new stiffening within the second compression stage. This similarity in slope is observed after the ASLS deforms by 0.275 mm with an applied force of 42 N, as well as by 0.31 mm with an applied force of 56 N. Furthermore, the shape of the F(x) curve related to "elastic creeping" is also highly similar for each compression-relaxation cycle (following 37 N, 42 N, and 56 N). In the case of one of ASLS measurements shown in Figure 13, the calculated stress σ (ε) could be interpolated as a linear proportionality $\sigma_{_after_initial_stiffening}$ (ε) = 1842·ε, which appears as 68.25% stiffer than in the initial compression stage ($\sigma_{_initial}$ =1095 N/mm^2·1.6825), E ≈ 1842 N/mm^2.

Upon exceeding the limit of the second compression stage (>55 N), the ASLS structure enters the third stage of deformation, characterized by a steeper slope of F(x) compared to the first stage. This stage culminates in the fracture of the first strut of the scaffold (a little bit above 1300 N). For the third compression stage, the experiment planned to determine the stiffening of the ASLS after reaching compression forces of 150 and 500 N. The compression and relaxation strokes were set at a speed of 1 mm/min, which is equivalent to 0.01667 mm/s (Figure 14).

During the fourth compression-relaxation cycle, the compression force limit was set to 150 N, resulting in a deformation of the ASLS structure of 0.41 mm. Subsequently, the ASLS structure was relaxed by lowering the compression force to 55 N (Figure 15). Once again, it should be noted that after relaxation, the ASLS is capable of withstanding compression up to 150 N, exhibiting almost linear proportionality between the stroke and reaction force. Hence, within this range of compression force, the ASLS deforms with full reversibility, acting as an elastic structure. This cycle led to a further increase in the elasticity modulus, which became approximately E ≈ 6278 N/mm^2. $\sigma_{_after_150N_stiffening}$ (ε) = 6278·ε, indicating an increase of approximately 260.55% compared to the second compression stage (1842 N/mm^2·2.6055).

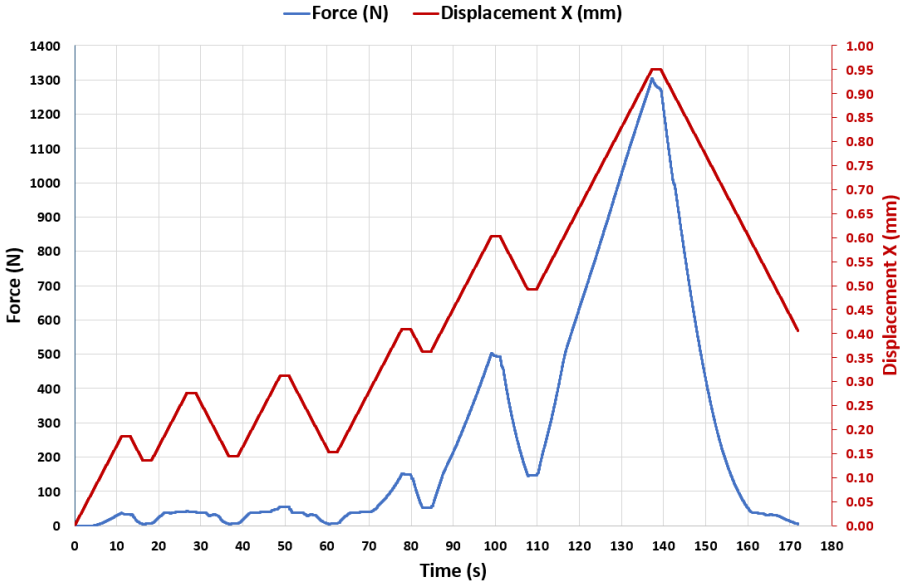


Figure 14. The diagram of changing the compression force and stroke versus time, in accordance with the experiment plan.

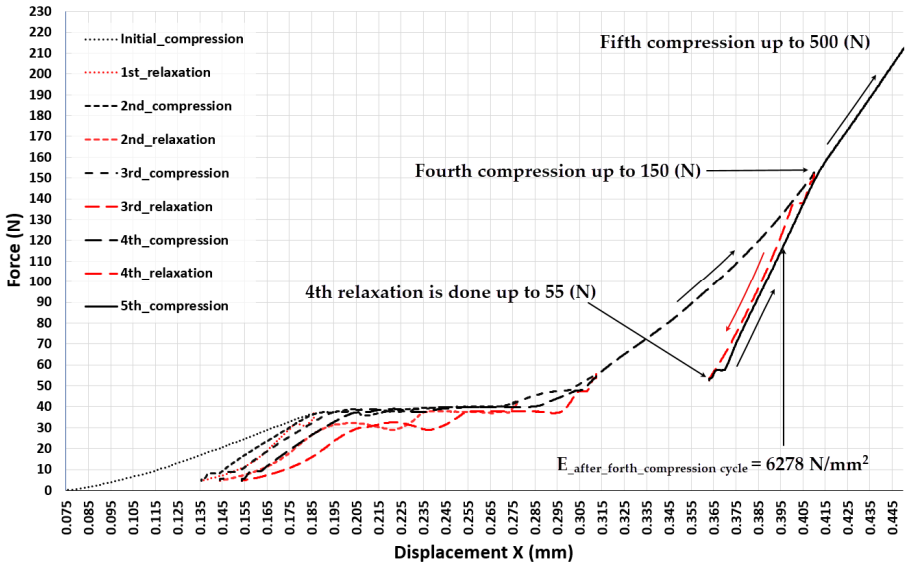


Figure 15. F(x) diagram with focus on complete fourth and beginning of the fifth compression-relaxation cycle. Black arrows, which are directed upwards, indicate compressive strokes, while the red ones, which are directed downwards, indicate relaxation strokes.

Within the fifth compression-relaxation cycle, a compression force of 500 N was applied, followed by relaxation of the ASLS structure to the level of the fourth cycle, i.e., down to 150 N (Figure 16). The outcomes of the fifth cycle were similar to the fourth cycle, with the ASLS acting as an elastic structure within the new force range. However, the elasticity modulus once again increased beyond the previous limit, reaching approximately $E \approx 9738\ N/mm^2$.

The final, sixth compression-relaxation cycle planned in the experiment featured a compression force limit of 1300 N, which is close to the ultimate strength of the ASLS structure (Figure 17). The force for the last relaxation step was set to reach 5 N. The maximal relative deformation of the ASLS achieved in this cycle was approximately 10% (between 9% and 10%). It is intriguing to consider why the ASLS structure straightens during relaxation, following a curve that encompasses both the second and first stages of

deformation. The final permanent or plastic deformation of the ASLS ranged from 0.395 to 0.415 mm, representing around 4% of the initial length of the ASLS.

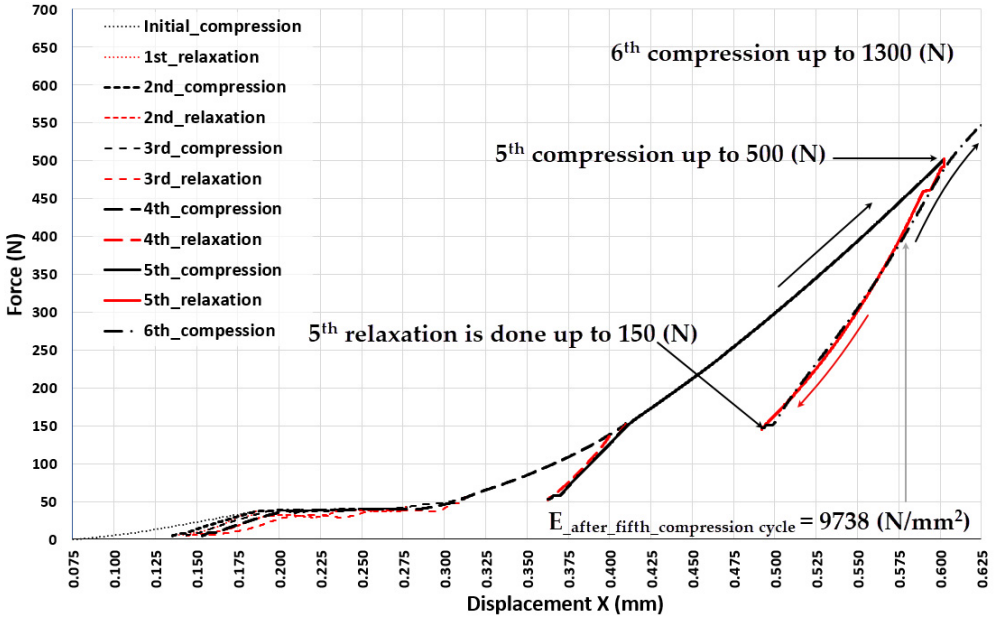


Figure 16. F(x) diagram with focus on complete fifth and beginning of the sixth compression-relaxation cycle. Black arrows, which are directed upwards, indicate compressive strokes, while the red ones, which are directed downwards, indicate relaxation strokes.

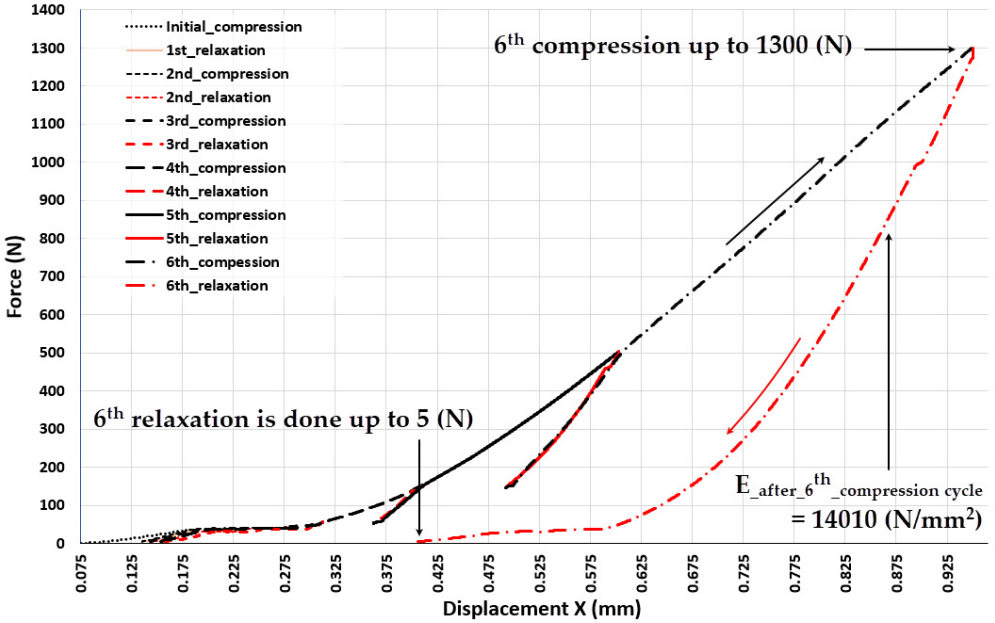


Figure 17. F(x) diagram with focus on the final, sixth compression-relaxation cycle. Black arrows, which are directed upwards, indicate compressive strokes, while the red ones, which are directed downwards, indicate relaxation strokes.

When the stroke of the pressure plates exceeds 1 mm (or 10% of the initial length of the scaffold) and the force becomes greater than 1300 N, the fracturing of the first struts becomes observable. This phenomenon is illustrated in the diagram, showing a sudden drop in the force-displacement curve (refer to Figure 18).

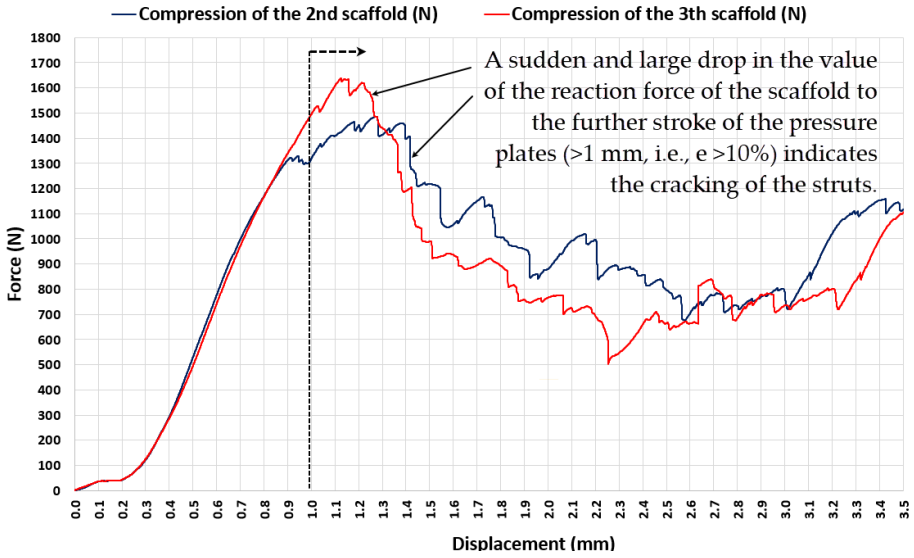


Figure 18. Diagram of reactive force of two ASLSs under compression load, focusing on deformation that exceeds 10% of the initial height (length) of the scaffold.

After deformation of 2.5 mm, the crushed scaffold struts are compacted in the scaffold space (Figure 19), and the resistance to further compression starts to increase again.

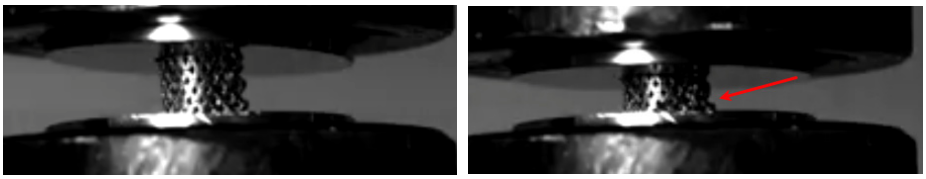
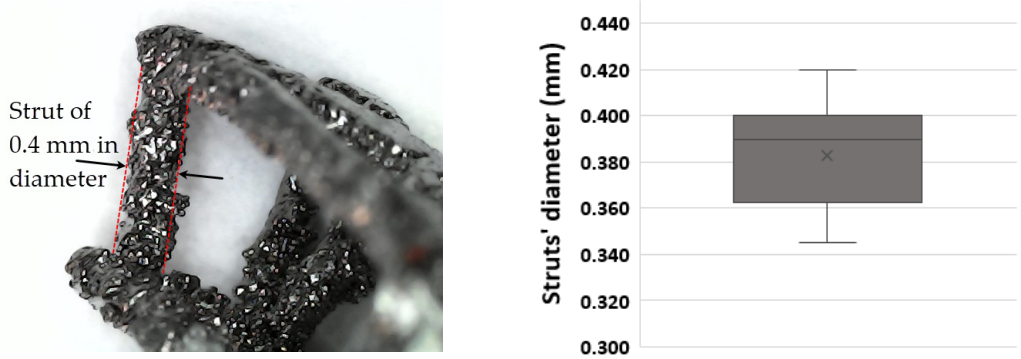


Figure 19. Two moments during the compressive deformation that exceeds 10% of the initial height of the scaffold.

The magnified image (Figure 20a) shows that the geometry of the scaffold strut, which was not subjected to the experiment, does not have the same shape as in the model. Instead of the expected round cross-section with a diameter of 0.4 mm, the struts exhibit a distinctive feature: They consist of numerous alloy pieces that have been hardened and joined using the EBM process.



(**a**) (**b**)

Figure 20. ASLS struts made through EBM in their real shape. (**a**) A magnified view of the scaffold strut, (**b**) error-bar diagram of the struts' thickness (diameter) based on 25 measurements (5 measurements of 5 struts of non-deformed ASLSs). The designed diameter is 0.4 mm.

For analyzing the cross-sections of the strut cuts at the locations where they were sectioned, magnified images have been included to document this specific aspect of the research and its outcomes. The attached figures display the fractured struts (refer to Figure 21).



Figure 21. The magnified (max. 1600×) view of fractured ASLS Struts: (**a**,**b**) views of the cross-section (colored by the red felt pen) of the fractured strut, (**c**) the magnified view of the strut's cross-section where it has been sheared off. The boundary of the cross-section is highlighted by an orange polyline.

By analyzing the measurements of the reaction force at discrete deformations of the ASLS and calculating the corresponding values of the modulus of elasticity, it becomes possible to determine the relationship between the compression force and the modulus of elasticity obtained through structure stiffening (Table 6).

Table 6. Correlation between ASLS deformation under the corresponding compression force and calculated modulus of elasticity of ASLS structure.

dx (mm)	F (N)	E (N/mm^2)
0.115	10	1095 [1]
0.185	37	1842
0.41	150	6278
0.6	500	9738
0.955	1300	14010

[1] Calculation based on F(x) of initial compression stroke, i.e., before stiffening.

By fitting a curve through the points obtained for the modulus of elasticity and the corresponding values of the compression (stiffening) force, it is feasible to interpolate this dependency as a logarithmic function (Figure 22).

$$E(F) = 4634.46 \cdot ln\left(0.115055 \cdot F_{stiffening} + 9.22071\right) - 9505.08, \quad (1)$$

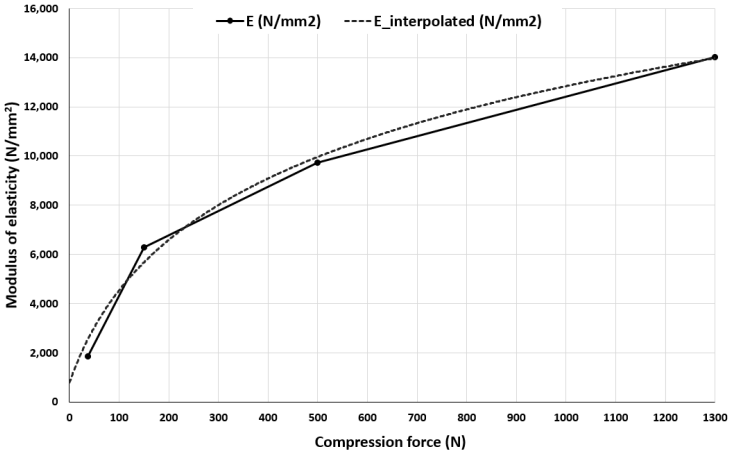


Figure 22. E(*F*)–Diagram that expresses the relation between the increase of modulus of elasticity and applied compression (stiffening) force.

By utilizing this approach, it becomes possible to adjust the required modulus of elasticity for a specific ASLS custom-designed for an individual patient. This allows for the rigidification of the ASLS in a manner that enables the desired elastic deformation of the ASLS under the patient-specific load.

4. Discussion

The compression testing conducted on the Ti6Al4V anatomically shaped lattice scaffolds (ASLS) produced using Electron Beam Melting (EBM) technology provided valuable insights into their mechanical behavior. The compression tests revealed distinct stages of compression and shed light on the scaffolds' deformation characteristics.

The results of the research largely align with existing studies, both in terms of the range of elastic modulus values for similar Ti6Al4V structures and in terms of the shape of the F(x) curve, i.e., $\sigma(\varepsilon)$ [24,39]. What sets this study apart from previous research is the focus on measuring the change in the elastic modulus of the lattice structure due to elastic-plastic deformation of the scaffold. Additionally, the study reveals characteristics of lattice kinds of scaffolds, such as ASLS, changing their mechanical properties when exposed to plastic deformation. This is especially interesting in the context of designing an anatomically shaped lattice scaffold, which is custom-designed for the specific missing piece of bone rather than a scaffold built using a generic 3D pattern of pores or struts.

The research confirmed the initial expectation that this type of scaffold can be adapted not only in design to match the anatomy of the missing (crushed) piece of bone but also to withstand the mechanical loads required during tissue recovery. It is evident that the design of anatomically shaped lattice scaffolds fabricated using EBM Ti6Al4V powder allows for a targeted increase in the modulus of elasticity by subjecting it to appropriate loading and plastic deformation. This implies that the ASLS, which are rigidified in this manner, can behave as an elastic structure, with deformation occurring within the target load limit and being nearly fully reversible. This feature is pivotal for the ossification process of the bone graft (a type of proto tissue) positioned within the scaffold cage during implantation. The appropriate elastic deformation of the scaffold enables the bone graft to withstand the intended pressure from the surrounding healthy bone tissue and initiates a bio-mechanical-electrical mechanism [40] that promotes the transformation of bone proto-tissue into mature bone tissue, fostering its growth and integration with the surrounding bone tissue. The specific compression-relaxation testing conducted on the ASLS scaffolds revealed the capability of the EBM Ti6Al4V lattice structure to rigidify in response to applied compression force and subsequent elastic-plastic deformation. These findings establish an experimentally determined relationship (similar to a logarithmic function) between the value of the modulus of elasticity and the compression force that enforces scaffold rigidification. However, it is important to remember that the paper focuses on a highly specific scaffold design, and therefore, the stiffening curve and demonstrated behavior are relevant only to a patient-specific ASLS. Nevertheless, these findings provide a valuable indication for future investigations into the Ti-alloys lattice structure phenomenon in bioengineering applications.

Considering the results presented here, along with the findings of other researchers who have conducted similar measurements [24], it is expected that research aimed at controlling the elasticity of titanium lattice structures—commonly made by EBM or DMLS additive manufacturing methods—particularly for the creation of patient-specific scaffolds for bone tissue recovery, needs to be intensified. The elastic modulus of an already-constructed lattice scaffold could be adjusted before implantation by applying proper compression, as demonstrated in this paper.

Furthermore, we can anticipate a series of studies that, utilizing outcomes, such as those presented in this paper, will facilitate the optimization of ASLS design in terms of mechanical characteristics through finite element analysis (FEA).

5. Conclusions

In conclusion, the findings from the research reported in this paper can be summarized as follows:

1. Lattice scaffolds, produced using the EBM additive manufacturing process with Ti6Al4V powder and intended for bone tissue recovery, exhibit the characteristic of plastic deformation even at low forces.
2. Prior to the stresses in the struts of the EBM-built lattice scaffold reaching a value that causes structural cracking, compression induces three distinctive stages of elastic-plastic deformation. The most intriguing phenomenon accompanying each of these deformation phases is the high degree of reversibility of the scaffold deformation after relaxation, although the force-elongation relationship shows significant nonlinearity. After the initial exposure of the scaffold to the upper limit of the load characteristic for each of these three phases of compression, the scaffold becomes stiffer compared to the state before that initial load, and each subsequent cycle of loading and relaxation in each range (characteristic for that phase) allows the scaffold to behave quasi-elastic (deformations are almost completely reversible). This feature is recognized as very useful for the situation where the stiffness of the lattice scaffold needs to be adjusted to the load generated by a specific patient during recovery, thus adjusting the deformation of the bone graft inside the scaffold in order to maximize the rate of the ossification process.
3. The stiffness of ASLSs already manufactured using EBM with Ti6Al4V can be changed (improved) by applying an appropriate compression (stiffening) load to it, thus achieving the target elasticity of the scaffold structure.
4. The research established a functional relationship between the compression (stiffening) force and the alteration in the elastic modulus of ASLS. Given that ASLS is a unique form of a lattice scaffold, the technique for measurement and data processing capable of determining this functional relationship, as showcased in the paper, holds a broader universal significance.

Author Contributions: Conceptualization, J.R.S. and M.S.; methodology, M.S. and J.A.; software, J.A. and R.T.; validation, D.M. and M.S.; formal analysis, J.A., R.T. and J.R.S.; investigation, J.R.S. and R.T.; resources, J.R.S.; data curation, M.S. and J.R.S.; writing—original draft preparation, J.R.S., M.S. and R.T.; writing—review and editing, M.S., D.M., J.R.S. and J.A.; visualization, M.S. and J.R.S.; supervision, D.M.; project administration, J.R.S. and D.M.; funding acquisition, M.S. All authors have read and agreed to the published version of the manuscript.

Funding: The research activities being financed by the Ministry of Science, Technological Development and Innovation of the Republic of Serbia (Contract No. 451-03-47/2023-01/200109).

Data Availability Statement: Not applicable.

Acknowledgments: The authors are grateful to Ministry of Science, Technological Development and Innovation of the Republic of Serbia for funding the research.

Conflicts of Interest: The authors declare no conflict of interest.

References

1. Trevisan, F.; Calignano, F.; Aversa, A.; Marchese, G.; Lombardi, M.; Biamino, S.; Ugues, D.; Manfredi, D. Additive manufacturing of titanium alloys in the biomedical field: Processes, properties and applications. *J. Appl. Biomater. Funct. Mater.* **2018**, *16*, 57–67. [CrossRef] [PubMed]
2. Jung, H.-D. Titanium and Its Alloys for Biomedical Applications. *Metals* **2021**, *11*, 1945. [CrossRef]
3. Sidhu, A.S. Surface Texturing of Non-Toxic, Biocompatible Titanium Alloys via Electro-Discharge. *Rep. Mech. Eng.* **2021**, *2*, 51–56. [CrossRef]
4. Turek, P.; Jońca, K.; Winiarska, M. Evaluation of the Accuracy of the Resection Template and Restorations of the Bone Structures in the Mandible Area Manufactured Using the Additive Technique. *Rep. Mech. Eng.* **2023**, *4*, 39–46. [CrossRef]

5. Van der Stok, J.; Van der Jagt, O.P.; Amin Yavari, S.; De Haas, M.F.; Waarsing, J.H.; Jahr, H.; Van Lieshout, E.M.; Patka, P.; Verhaar, J.A.; Zadpoor, A.A.; et al. Selective laser melting-produced porous titanium scaffolds regenerate bone in critical size cortical bone defects. *J. Orthop. Res.* **2013**, *31*, 792–799. [CrossRef]
6. Sing, S.L.; An, J.; Yeong, W.Y.; Wiria, F.E. Laser and electron-beam powder-bed additive manufacturing of metallic implants: A review on processes, materials and designs. *J. Orthop. Res.* **2016**, *34*, 369–385. [CrossRef]
7. Liu, S.; Shin, Y.C. Additive manufacturing of Ti6Al4V alloy: A review. *Mater. Des.* **2019**, *164*, 107552. [CrossRef]
8. Tamayo, J.A.; Riascos, M.; Vargas, C.A.; Baena, L.M. Additive manufacturing of Ti6Al4V alloy via electron beam melting for the development of implants for the biomedical industry. *Heliyon* **2021**, *7*, e06892. [CrossRef]
9. Dabrowski, B.; Swieszkowski, W.; Godlinski, D.; Kurzydlowski, K.J. Highly porous titanium scaffolds for orthopaedic applications. *J. Biomed. Mater. Res. Part B Appl. Biomater.* **2010**, *95*, 53–61. [CrossRef]
10. Tshephe, T.S.; Akinwamide, S.O.; Olevsky, E.; Olubambi, P.A. Additive manufacturing of titanium-based alloys—A review of methods, properties, challenges, and prospects. *Heliyon* **2022**, *8*, e09041. [CrossRef]
11. Acquesta, A.; Monetta, T. As-Built EBM and DMLS Ti-6Al-4V Parts: Topography–Corrosion Resistance Relationship in a Simulated Body Fluid. *Metals* **2020**, *10*, 1015. [CrossRef]
12. Hu, J.; Wang, Y.; Fan, M.; Yao, Q.; Zheng, P. The comparison of properties of Ti-6Aluminum-4Vanadium porous scaffolds fabricated through low-power selective laser Melting and electron beam melting. *Digit. Med.* **2022**, *8*, 12. [CrossRef]
13. Milovanović, J.; Stojković, M.; Trifunović, M.; Vitković, N. Review of Bone Scaffold Design Concepts and Design Methods. *Facta Univ. Ser. Mech. Eng.* **2023**, *21*, 151–173. [CrossRef]
14. Li, B.; Hesar, B.D.; Zhao, Y.; Ding, L. Design and additive manufacturing of porous titanium scaffolds for optimum cell viability in bone tissue engineering. *Proc. Inst. Mech. Eng. Part B J. Eng. Manuf.* **2020**. [CrossRef]
15. Gürkan, D.; Sagbas, B.; Dalbayrak, B. Investigating mechanical and biological properties of additive manufactured Ti6Al4V lattice structures for orthopedic implants. *J. Mater. Res.* **2023**, *38*, 507–518. [CrossRef]
16. Hudák, R.; Schnitzer, M.; Králová, Z.O.; Gorejová, R.; Mitrík, L.; Rajťúková, V.; Tóth, T.; Kovačević, M.; Riznič, M.; Oriňaková, R.; et al. Additive Manufacturing of Porous Ti6Al4V Alloy: Geometry Analysis and Mechanical Properties Testing. *Appl. Sci.* **2021**, *11*, 2611. [CrossRef]
17. Bari, K. Design, Simulation, and Mechanical Testing of 3D-Printed Titanium Lattice Structures. *J. Compos. Sci.* **2023**, *7*, 32. [CrossRef]
18. Galarraga, H.; Lados, D.A.; Dehoff, R.R.; Kirka, M.M.; Nandwana, P. Effects of the microstructure and porosity on properties of Ti-6Al-4V ELI alloy fabricated by electron beam melting (EBM). *Addit. Manuf.* **2016**, *10*, 47–57. [CrossRef]
19. Distefano, F.; Pasta, S.; Epasto, G. Titanium Lattice Structures Produced via Additive Manufacturing for a Bone Scaffold: A Review. *J. Funct. Biomater.* **2023**, *14*, 125. [CrossRef]
20. Raheem, A.A.; Hameed, P.; Whenish, R.; Elsen, R.S.; G, A.; Jaiswal, A.K.; Prashanth, K.G.; Manivasagam, G. A Review on Development of Bio-Inspired Implants Using 3D Printing. *Biomimetics* **2021**, *6*, 65. [CrossRef]
21. Mondal, P.; Das, A.; Mondal, A.; Chowdhury, A.R.; Karmakar, A. Fabrication of Ti-6Al-4V Porous Scaffolds Using Selective Laser Melting (SLM) and Mechanical Compression Test for Biomedical Applications. *J. Inst. Eng. (India) Ser. D* **2022**, *103*, 181–190. [CrossRef]
22. Loginov, Y.N.; Koptyug, A.; Popov, V.V.; Belikov, S.V.; Mukanov, G.; Golodnov, A.I.; Stepanov, S.I. Compression deformation and fracture behavior of additively manufactured Ti–6Al–4V cellular structures. *Int. J. Lightweight Mater. Manuf.* **2022**, *5*, 126–135. [CrossRef]
23. Dhiman, S.; Singh, M.; Sidhu, S.S.; Bahraminasab, M.; Pimenov, D.Y.; Mikolajczyk, T. Cubic Lattice Structures of Ti6Al4V under Compressive Loading: Towards Assessing the Performance for Hard Tissue Implants Alternative. *Materials* **2021**, *14*, 3866. [CrossRef]
24. Zhang, C.; Zhang, L.; Liu, L.; Lv, L.; Gao, L.; Liu, N.; Wang, X.; Ye, J. Mechanical behavior of a titanium alloy scaffold mimicking trabecular structure. *J. Orthop. Surg. Res.* **2020**, *15*, 40. [CrossRef]
25. Del Guercio, G.; Galati, M.; Saboori, A.; Fino, P.; Iuliano, L. Microstructure and Mechanical Performance of Ti–6Al–4V Lattice Structures Manufactured via Electron Beam Melting (EBM). *Acta Metall. Sin. (Engl. Lett.)* **2020**, *33*, 183–203. [CrossRef]
26. Kotzem, D.; Arold, T.; Bleicher, K.; Raveendran, R.; Niendorf, T.; Walther, F. Ti6Al4V lattice structures manufactured by electron beam powder bed fusion—Microstructural and mechanical characterization based on advanced in situ techniques. *J. Mater. Res. Technol.* **2023**, *22*, 2111–2130. [CrossRef]
27. Parthasarathy, J.; Starly, B.; Raman, S.; Christensen, A. Mechanical evaluation of porous titanium (Ti6Al4V) structures with electron beam melting (EBM). *J. Mech. Behav. Biomed. Mater.* **2010**, *3*, 249–259. [CrossRef]
28. Zumofen, L.; Kopanska, K.S.; Bono, E.; Kirchheim, A.; De Haller, E.B.; Graf-Hausner, U. Properties of additive-manufactured open porous titanium structures for patient-specific load-bearing implants. *Front. Mech. Eng.* **2022**, *7*, 830126. [CrossRef]
29. De Pasquale, G.; Luceri, F.; Riccio, M. Experimental Characterization of SLM and EBM Cubic Lattice Structures for Lightweight Applications. *Exp. Mech.* **2019**, *59*, 469–482. [CrossRef]
30. Sepe, R.; De Luca, A.; Giannella, V.; Borrelli, R.; Franchitti, S.; Di Caprio, F.; Caputo, F. Influence of dimension, building position, and orientation on mechanical properties of EBM lattice Ti6Al4V trusses. *Int. J. Adv. Manuf. Technol.* **2022**, *122*, 3183–3198. [CrossRef]

31. Suard, M.; Martin, G.; Lhuissier, P.; Dendievel, R.; Vignat, F.; Blandin, J.-J.; Villeneuve, F. Mechanical equivalent diameter of single struts for the stiffness prediction of lattice structures produced by Electron Beam Melting. *Addit. Manuf.* **2015**, *8*, 124–131. [CrossRef]
32. Cansizoglu, O.; Harrysson, O.; Cormier, D.; West, H.; Mahale, T. Properties of Ti-6Al-4V non-stochastic lattice structures fabricated via electron beam melting. *Mater. Sci. Eng. A* **2008**, *492*, 468–474. [CrossRef]
33. Del Guercio, G.; Galati, M.; Saboori, A. Innovative Approach to Evaluate the Mechanical Performance of Ti–6Al–4V Lattice Structures Produced by Electron Beam Melting Process. *Met. Mater. Int.* **2021**, *27*, 55–67. [CrossRef]
34. Ataee, A.; Li, Y.; Fraser, D.; Song, G.; Wen, C. Anisotropic Ti-6Al-4V gyroid scaffolds manufactured by electron beam melting (EBM) for bone implant applications. *Mater. Des.* **2018**, *137*, 345–354. [CrossRef]
35. Galati, M.; Saboori, A.; Biamino, S.; Calignano, F.; Lombardi, M.; Marchiandi, G.; Minetola, P.; Fino, P.; Iuliano, L. Ti-6Al-4V lattice structures produced by EBM: Heat treatment and mechanical properties. *Procedia CIRP* **2020**, *88*, 411–416. [CrossRef]
36. Milovanovic, J.; Stojković, M.; Husain, K.; Korunovic, N.; Arandjelovic, J. Holistic Approach in Designing the Personalized Bone Scaffold: The Case of Reconstruction of Large Missing Piece of Mandible Caused by Congenital Anatomic Anomaly. *J. Healthc. Eng.* **2020**, *2020*, 6689961. [CrossRef] [PubMed]
37. Stojkovic, M.; Korunovic, N.; Trajanovic, M.; Milovanovic, J.; Trifunovic, M.; Vitkovic, N. Design study of Anatomically Shaped Latticed Scaffolds for the bone tissue recovery. In Proceedings of the III South-East European Conference on Computational Mechanics-SEECCM III, Kos Island, Greece, 12–14 June 2013.
38. Korunovic, N.; Trajanovic, M.; Stevanovic, D.; Vitkovic, N.; Stojkovic, M.; Milovanovic, J.; Ilic, D. Material characterization issues in FEA of long bones. In Proceedings of the SEECCM III—3rd South-East European Conference on Computational Mechanics, Kos Island, Greece, 12–14 June 2013.
39. Ashby, M.F. The properties of foams and lattices. *Philos. Trans. Ser. A Math. Phys. Eng. Sci.* **2006**, *364*, 15–30. [CrossRef]
40. Khare, D.; Basu, B.; Dubey, A.K. Electrical stimulation and piezoelectric biomaterials for bone tissue engineering applications. *Biomaterials* **2020**, *258*, 120280. [CrossRef]

Disclaimer/Publisher's Note: The statements, opinions and data contained in all publications are solely those of the individual author(s) and contributor(s) and not of MDPI and/or the editor(s). MDPI and/or the editor(s) disclaim responsibility for any injury to people or property resulting from any ideas, methods, instructions or products referred to in the content.